A proposal for detecting the spin of a single electron in superfluid helium

Jinyong Ma,[1] Y. S. S. Patil,[1] Jiaxin Yu,[2] Yiqi Wang,[2] and J. G. E. Harris[1, 2, 3, *]

[1]*Department of Physics, Yale University, New Haven, Connecticut 06520, USA*
[2]*Department of Applied Physics, Yale University, New Haven, Connecticut 06520, USA*
[3]*Yale Quantum Institute, Yale University, New Haven, Connecticut 06520, USA*
(Dated: August 15, 2023)

The electron bubble in superfluid helium has two degrees of freedom that may offer exceptionally low dissipation: the electron's spin and the bubble's motion. If these degrees of freedom can be read out and controlled with sufficient sensitivity, they would provide a novel platform for realizing a range of quantum technologies and for exploring open questions in the physics of superfluid helium. Here we propose a practical scheme for accomplishing this by trapping an electron bubble inside a superfluid-filled opto-acoustic cavity.

Atom-like defects in a solid can serve as quantum systems with low dissipation, strong coupling to external fields, and compatibility with well-established readout and control schemes. Defects that combine these features have been used in a range of applications, for example as quantum memories, single-photon sources, and as detectors that combine high sensitivity and spatial resolution. The performance of these systems is partially determined by the defect's internal properties, such as its level structure and its coupling to various fields. It is also determined by the properties of the host material, which represents a potential source of dissipation and noise [1].

Very long coherence times have been realized in a number of defect systems, including E′ centers in SiO_2 [2], N- or Si-vacancy centers in diamond [3, 4], and electrons trapped at Si/SiO_2 interfaces [5]. These systems have been integrated with a range of readout schemes (including magnetic resonance force microscopy (MRFM) [2], nanoscale superconducting quantum interface devices [6], and laser excitation and fluorescence emission [4]), and have facilitated the emergence of defect-based quantum sensing [7], computing [8] and information processing [9, 10].

One atom-like defect that possesses a number of remarkable properties is the electron bubble (EB), which forms when a single electron is immersed in superfluid He. Such an electron resides inside a spherical bubble with radius 1.9 nm [11]. This system differs from quantum defects in solid hosts in a number of respects. First, it is free to move, and at sufficiently low temperature it travels ballistically through the superfluid host. Second, the host material (i.e., superfluid He) is itself the topic of a number of outstanding questions that can be explored using EBs. These include the mechanical properties of vortices, and the onset and decay of turbulence [12–18]. A third notable feature of this system is that the host material offers a near-total absence of magnetic degrees of freedom, which is expected to result in remarkably long spin coherence times for an isolated EB. By way of illustration, the predicted T_1 for an EB in solid ^{3}He is ∼ 10^5 s [19, 20], limited by the hyperfine interaction between the electron and the spins of the ^{3}He nuclei surrounding the bubble. Even greater T_1 may be achieved for an EB in ^{4}He (which has no nuclear spin). To date, T_1 has not been measured for an isolated EB. Only a lower bound ($T_1 > 100$

ms) has been estimated from electron spin resonance (ESR) studies of EB ensembles [21, 22].

Here we propose a scheme for efficiently detecting and manipulating the spin of a single EB in superfluid He. In this scheme, the EB is trapped by an acoustic standing wave. A magnetic field gradient transduces the electron's spin state to the EB's motion within the trap, which in turn is monitored via an optical cavity. This approach may be viewed as analogous to MRFM (in the sample-on-cantilever configuration) [23]: here the sample is the electron, and the role of the cantilever is played by the trapped bubble. Many of the parameters of the device proposed here (such as its mechanical resonance frequency, operating temperature, and quality factor) are similar to those of cantilever-based MRFM devices [23]. However the effective mass of the EB [24] is ∼ 10^{-14} that of typical MRFM cantilevers, resulting in a high signal-to-noise ratio (SNR) for measurements of the electron's spin. We emphasize that each of the components required for this scheme has already been demonstrated [25–29], indicating the feasibility of using this system to access new regimes of both defect-based sensing and superfluid physics.

This scheme may be realized in a variety of ways, but for concreteness we focus on an implementation based on the superfluid-filled cavities described in Ref. [26, 29] and illustrated in Fig. 1. The cavity (with length $L_{cav} = 100$ μm) is formed between the end faces of two optical fibers that have each been fabricated with a concave surface and coated with high-reflectivity dielectric mirrors [30]. When filled with superfluid He at temperature $T < 100$ mK, these cavities have been shown to confine optical modes with finesse $\mathcal{F} = 10^5$ (for vacuum wavelength $\lambda_{opt} = 1550$ nm) and acoustic modes with quality factor $Q_{ac} = 10^5$ (for wavelength $\lambda_{ac} = 775$ nm).

The EB is generated by field emission from a metal tip [25] positioned close to the cavity, and trapped by driving one of the cavity's acoustic modes to a large amplitude. As described in Ref. [31], the EB is attracted to the density antinodes of the resulting standing wave. Fig. 2(a) shows the potential $U(z)$ experienced by an EB in a standing wave with amplitude $\delta\rho_{He}/\rho_{He} = 2 \times 10^{-3}$ where $\delta\rho_{He}$ is the change in the He density and $\rho_{He} = 145$ kg/m^3 is the equilibrium density of superfluid He. This value of $\delta\rho_{He}/\rho_{He}$ is chosen to give a trap depth $U_0/k_B = 300$ mK, a factor of 10 greater than the
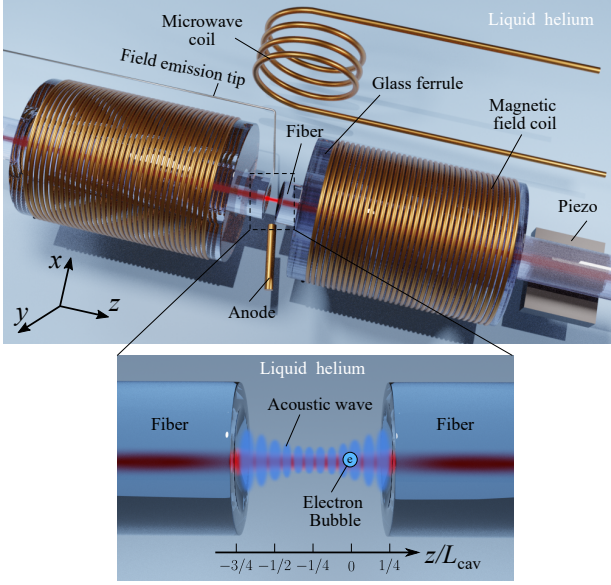
FIG. 1. Schematic illustration of the proposed setup. The entire region is filled with superfluid He. An electron bubble (EB) is produced by field emission from a metal tip located near a cavity formed between two optical fibers. An acoustic standing wave in the cavity (inset, blue) traps the EB. A microwave coil is used to manipulate the electron's spin. A magnetic field gradient (generated by the field coil) transduces the state of electron's spin to the EB's displacement, which is measured using an optical mode of the cavity (inset, red).

operating temperature ($T = 30$ mK, as discussed below). It can be generated in an acoustic mode with $Q_{ac} = 10^5$ and resonant frequency $\omega_{ac}/2\pi = 320$ MHz [29] (corresponding to $\lambda_{ac} = 775$ nm) by driving one of the fiber ends to an amplitude ~ 2 fm with an ultrasonic transducer [28]. It results in a trap frequency (i.e., of the EB's center-of-mass motion) $\omega_{EB}/2\pi = 2.9$ MHz.

The acoustic trap can be characterized even in the absence of an EB. This is because the density modulation produced by an acoustic mode causes a large detuning of the cavity optical mode with $2n_{opt} = n_{ac}$, were n_{opt} (n_{ac}) is the number of optical (acoustic) half-wavelengths fitting in the cavity (all other optical modes are only weakly coupled to this acoustic mode [26]). For the particular device considered here, we take $n_{ac} = 258$. The acoustic trap is monitored using the optical mode with $n_{opt} = 129$. In this case the acoustic trap modulates the optical mode with depth 190κ (where $\kappa = 15$ MHz is the linewidth of the optical mode) which should be straightforward to measure [31].

The EB's displacement around the minimum of $U(z)$ is monitored using an optical mode. Since the EB's index of refraction differs from that of the He filling the cavity, it alters the optical length of any optical mode by an amount proportional to the overlap between the mode and the EB [32, 33]. The single-photon coupling rate [34] g_0 arising from this interaction is optimized for an optical mode whose intensity gradient is maximum at the EB's equilibrium position. For the sake of specificity, we consider an EB trapped at a distance $L_{cav}/4$

from one of the mirrors (see inset of Fig. 1), and readout using the optical mode with $n_{opt} = 130$ (Fig. 2(b,c)).
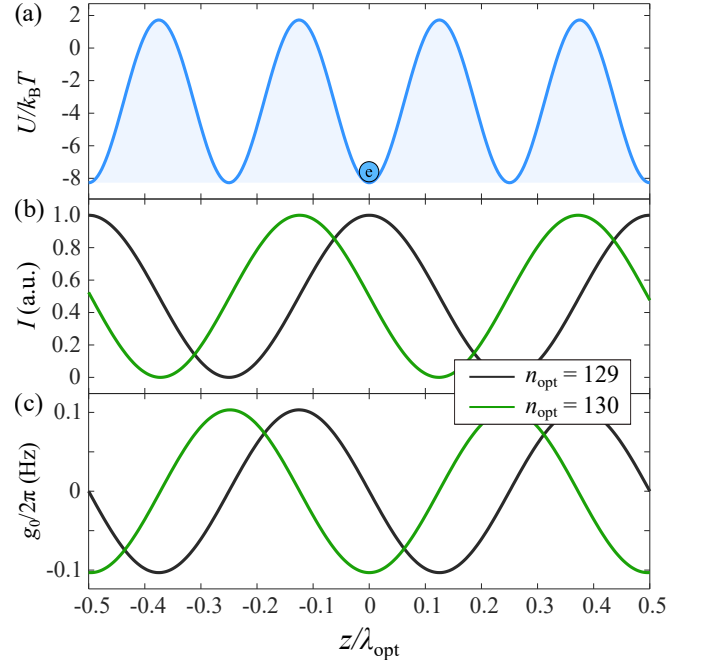

FIG. 2. (a) The potential $U(z)$ experienced by an EB in the acoustic standing wave described in the text. The blue circle indicates the EB's equilibrium position. (b) The intensity $I(z)$ of two optical modes. Black: the mode used to monitor the acoustic trap ($n_{opt} = 129$). Green: the mode used to detect the EB motion ($n_{opt} = 130$). (c) The optomechanical coupling rates g_0 of the two optical modes shown in (b). The horizontal axis denotes the EB position z relative to the point one-quarter of the way between the cavity mirrors (see Fig. 1 (inset)).

For the temperature range considered here ($T < 100$ mK), damping of the EB motion is primarily due to collisions with thermal phonons and impurity ^{3}He atoms. Both processes are well-studied [35–37], and Fig. 3 shows the quality factor $Q_{EB}(T)$ of the EB's motion calculated for an EB trapped in the potential of Fig. 2(a) [31]. At higher T the damping is dominated by thermal phonons, while ^{3}He impurities dominate for lower T. Fig. 3 shows calculations for the ^{3}He concentration x_3 ranging from the natural abundance ($x_3 \sim 1$ ppm) to the lowest level that is commercially available ($x_3 = 10^{-6}$ ppm).

The access to the EB's motion provided by the optical cavity can be exploited to study the spin of the EB. In particular, the state of the electron spin can be transduced by applying a magnetic field gradient of magnitude G, which results in a force of magnitude $F_{mag} = \mu_s G$ on the EB, where μ_s is the electron's magnetization along the gradient. In the scheme proposed here, a pair of coils wound around the ferrules (Fig. 1) produces a field along z with magnitude B_0 and gradient (along z) G. A separate microwave coil is used to drive the electron's spin resonance.

We consider three protocols for measuring the EB spin. Each operates by causing F_{mag} to oscillate with frequency ω_{EB} and then measuring the EB's resulting motion. In Protocol I, G
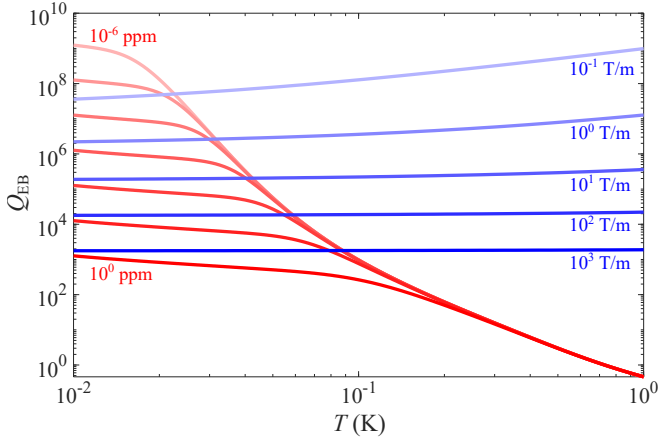
FIG. 3. Requirements for sensing the spin of a single EB. Blue curves: the value of Q_{EB} required to obtain SNR = 1 in a 1 s measurement, assuming $P = 1$ μW and $\mathcal{F} = 10^5$. Each curve corresponds to the indicated value of the magnetic field gradient G. Red curves: $Q_{EB}(T)$ for $x_3 = 10^{-6}, 10^{-5}, ..., 10^{-1}, 1$ ppm. Blue and red curves cross at the value of T below which the corresponding x_3 and G would result in SNR > 1.

is modulated while μ_s is constant. In Protocols II & III, μ_s is modulated while G is constant. In each case the amplitude of the signal (in the force domain) is simply $\mu_s G$ (taking the static value of μ_s and the oscillation amplitude of G in Protocol I, and *vice versa* in Protocols II & III). Because these three protocols are subject to the same noise sources (see below), it is straightforward to estimate the SNR for each of them. In practice, each protocol is limited by different technical constraints, which we consider next. A more detailed description of each protocol is in Ref. [31].

Protocol I is simply to modulate G at frequency ω_{EB}. The amplitude of the resulting EB displacement is shown in Fig. 4(a) as a function of G and Q_{EB}. In this protocol no microwave tone is applied, and B_0 plays no direct role.

Protocol II uses the electron spin's Rabi oscillation to produce an oscillating F_{mag}. In this case G and B_0 are fixed, and a microwave magnetic field with amplitude B_1 drives the transition between the spin states, whose Zeeman splitting is produced by B_0. This results in $\mu_s(t) = \mu_B \left(\frac{\omega_1}{\Omega}\right)^2 \sin^2\left(\frac{\Omega t}{2}\right)$, where $\Omega = (\Delta^2 + \omega_1^2)^{1/2}$ is the Rabi frequency, Δ is the detuning between the microwave drive and the Zeeman splitting, $\omega_1 = \frac{\mu_B g}{\hbar} B_1$, g is the electron g-factor, and μ_B is the Bohr magneton. Requiring $\Omega = \omega_{EB}$ (so as to drive the EB motion resonantly) fixes Δ for a chosen B_1, as shown by the grey curve of Fig. 4(b). The amplitude of the resulting EB displacement is shown by the green curves of Fig. 4(b).

Protocol III is analogous to the one used in Refs. [2, 27]. It uses constant a G and modulates the uniform field so that $B_0(t) = \bar{B}_0 + B_{mod}\sin(\omega_{EB}t)$. In addition, a fixed microwave tone with amplitude B_1 and frequency $\omega_0 = g\mu_B \bar{B}_0/\hbar$ is applied. As a result, the Zeeman splitting passes through resonance with the microwaves twice per period of the modulation. If the condition for adiabaticity is met for each of these pas-
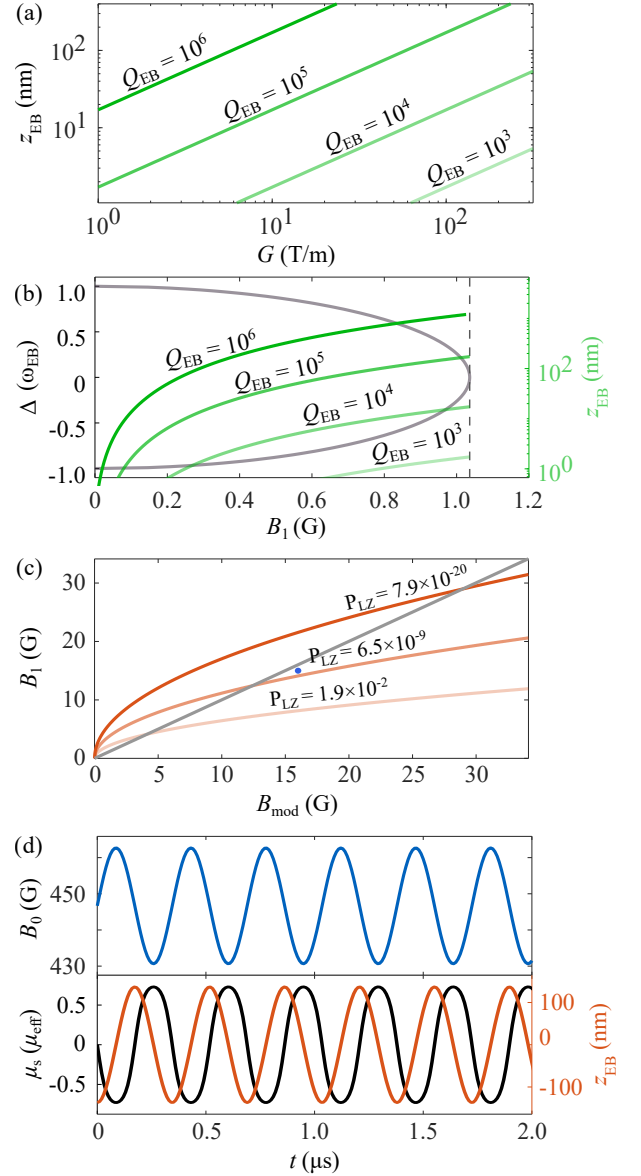

FIG. 4. Three protocols for single spin detection. (a) Protocol I. The amplitude of the EB displacement z_{EB} as a function of the amplitude of G. (b) Protocol II. Gray curve: the detuning $\Delta(B_1)$ that ensures the Rabi oscillations drive the EB motion resonantly (with $B_0 = 450$ G). Green curve: $z_{EB}(B_1)$. Dashed line: the maximum value of B_1 for this protocol. (c) Protocol III. Red curves: contours of constant error rates for the adiabatic passage described in the text. Gray line: the condition $B_1 = B_{mod}$. (d) The timing for Protocol III, assuming $B_1 = 15$ G and $B_{mod} = 16$ G, indicated by the blue dot in (c). Panels (c),(d) assume $\bar{B}_0 = 450$ G and $Q_{EB} = 6 \times 10^5$.

sages, the magnetization is given by [27]

$$\mu_s(t) = \pm\mu_{eff} \frac{B_{mod}\sin(\omega_{EB}t)}{\left(B_1^2 + B_{mod}^2 \sin^2(\omega_{EB}t)\right)^{1/2}} \quad (1)$$

where $\mu_{eff} = g\mu_B/2$. This signal is maximized when $B_{mod} > B_1$ (the region to the right of the gray line in Fig. 4(c)).

The probability that $\mu_s(t)$ follows this form during an individ-

ual passage is $1 - P_{LZ}$, where $P_{LZ} = \exp(-\pi\mu_{eff}B_1^2/\hbar\omega_{EB}B_{mod})$ [31] is the well-known Landau-Zener formula. The red curves in Fig. 4(c) show countours of B_1 and B_{mod} corresponding to various values of P_{LZ}. The region above the middle curve corresponds to parameters for which a diabatic error (i.e., in which μ_s does not follow Eq. 1) occurs less than once per 100 s. Fig. 4(d) shows the timing of this protocol for $B_1 = 15$ G and $B_{mod} = 16$ G (corresponding to the blue point in Fig. 4(c)).
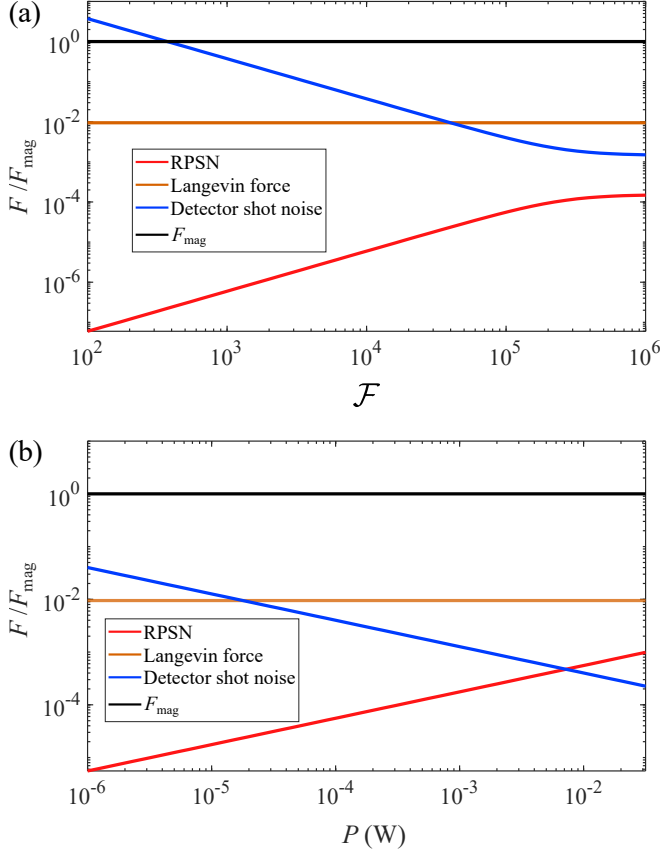

FIG. 5. The estimated signal and noise for single-spin detection. (a) Three noise sources F (expressed as forces) compared with the signal F_{mag}, all as a function of the cavity finesse $\mathcal{F}$ and for input laser power $P = 100$ μW. For $\mathcal{F} > 10^5$ the red and blue curves deviate from linear as the system approaches the resolved-sideband regime. (b) The same as (a), but as a function of P for $\mathcal{F} = 10^5$. The intersection of the red and blue curves near $P = 8$ mW corresponds to the standard quantum limit. Both (a) and (b) assume $x_3 = 10^{-3}$ ppm and $T = 30$ mK (corresponding to $Q_{EB} = 6 \times 10^5$, see Fig. 3), and $G = 100$ T/m.

To estimate the feasibility of these protocols, we consider the following noise sources: the Langevin force exerted by the thermal bath, the radiation pressure shot noise (RPSN) exerted by the photons in the optical mode, and the detector's shot noise (we assume the cavity detuning is monitored via heterodyne detection of the light from the cavity mode with $n_{opt} = 130$). These noise sources are described in detail in Ref. [31], and typical contributions from each are shown in Fig. 5.

For a wide range of experimental parameters, the noise sources that make the greatest contribution to the heterodyne signal are the EB's thermal motion and the detector's shot noise (many MRFM experiments also operate in this regime [2, 23, 38]). In this regime, the signal-to-noise ratio is SNR = $F_{mag}/\sqrt{2}(F_{th} + F_{shot})$, where

$$F_{th} = \sqrt{4k_B T m_{EB}\omega_{EB}b/Q_{EB}} \qquad (2)$$

$$F_{shot} = \hbar\omega_{EB}|\kappa/2 - i\omega_{EB}|\frac{\kappa}{\kappa_{ex}}\sqrt{\frac{bm_{EB}\omega_{EB}\omega_l}{8PQ_{EB}^2 g_0^2}} \qquad (3)$$

Here $m_{EB} = 1.6 \times 10^{-24}$ kg is the effective mass of the EB [24], b is the measurement bandwidth, $\omega_l = 2\pi c/\lambda_{opt}$ and κ_{ex} is the external coupling rate of the optical cavity (the calculations shown in Figs. 3,5 assume $\kappa_{ex} = 0.44\kappa$).

In Fig. 3, the blue lines show the value of Q_{EB} required to achieve SNR = 1 with $b = 1$ Hz. Each blue line corresponds to a different value of G (which should be interpreted as the amplitude of the modulated gradient in Protocol I, and as the static gradient in Protocols II & III). We note that the values of G considered in Fig. 3 are orders of magnitude lower than is typically required for single-electron MRFM [2, 23, 38]. The choice of $b = 1$ Hz should be feasible owing to the long coherence time expected for the EB spin (and, for Protocol III, the ability to ensure that diabatic transitions occur much less than once per second).

In conclusion, we have presented a scheme to manipulate and detect the spin of an individual EB trapped in a cavity that is filled with superfluid He. This approach combines well-established techniques to produce, manipulate, and sense the electron spin, and should allow for the EB to be employed analogously to other atom-like defects. The unique features of this system (in particular, the EB's mobility and long spin coherence) may open new opportunities in high-sensitivity magnetometry, and in the study of superfluid He.

* jack.harris@yale.edu

[1] G. Wolfowicz, F. J. Heremans, C. P. Anderson, S. Kanai, H. Seo, A. Gali, G. Galli, and D. D. Awschalom, Nature Reviews Materials 6, 906 (2021).
[2] D. Rugar, R. Budakian, H. J. Mamin, and B. W. Chui, Nature 430, 329 (2004).
[3] F. Jelezko, T. Gaebel, I. Popa, A. Gruber, and J. Wrachtrup, Physical Review Letters 92, 076401 (2004).
[4] T. Schröder, M. E. Trusheim, M. Walsh, L. Li, J. Zheng, M. Schukraft, A. Sipahigil, R. E. Evans, D. D. Sukachev, C. T. Nguyen, J. L. Pacheco, R. M. Camacho, E. S. Bielejec,

M. D. Lukin, and D. Englund, Nature Communications **8**, 15376 (2017).

[5] M. Xiao, I. Martin, E. Yablonovitch, and H. W. Jiang, Nature **430**, 435 (2004).

[6] D. Vasyukov, Y. Anahory, L. Embon, D. Halbertal, J. Cuppens, L. Neeman, A. Finkler, Y. Segev, Y. Myasoedov, M. L. Rappaport, M. E. Huber, and E. Zeldov, Nature Nanotechnology **8**, 639 (2013).

[7] J. M. Taylor, P. Cappellaro, L. Childress, L. Jiang, D. Budker, P. R. Hemmer, A. Yacoby, R. Walsworth, and M. D. Lukin, Nature Physics **4**, 810 (2008).

[8] J. R. Weber, W. F. Koehl, J. B. Varley, A. Janotti, B. B. Buckley, C. G. Van de Walle, and D. D. Awschalom, Proceedings of the National Academy of Sciences **107**, 8513 (2010).

[9] J. Wrachtrup and F. Jelezko, Journal of Physics: Condensed Matter **18**, S807 (2006).

[10] C. E. Bradley, J. Randall, M. H. Abobeih, R. C. Berrevoets, M. J. Degen, M. A. Bakker, M. Markham, D. J. Twitchen, and T. H. Taminiau, Physical Review X **9**, 031045 (2019).

[11] Y. Xing and H. J. Maris, Journal of Low Temperature Physics **201**, 634 (2020).

[12] V. N. Popov, Sov. Phys. JETP **37** (1973).

[13] J.-M. Duan and A. J. Leggett, Phys. Rev. Lett. **68**, 1216 (1992).

[14] J.-M. Duan, Phys. Rev. B **49**, 12381 (1994).

[15] G. Baym and E. Chandler, Journal of Low Temperature Physics **50**, 57 (1983).

[16] E. Kozik and B. Svistunov, Physical Review Letters **92**, 035301 (2004).

[17] W. F. Vinen, M. Tsubota, and A. Mitani, Physical Review Letters **91**, 135301 (2003).

[18] P. M. Chesler, H. Liu, and A. Adams, Science **341**, 368 (2013).

[19] C.-Y. Huang, Physics Letters A **34**, 225 (1971).

[20] W. Yao, arXiv:cond-mat/0510757 (2005), arXiv:cond-mat/0510757.

[21] J. F. Reichert and A. J. Dahm, Physical Review Letters **32**, 271 (1974).

[22] P. H. Zimmermann, J. F. Reichert, and A. J. Dahm, Physical Review B **15**, 2630 (1977).

[23] C. L. Degen, M. Poggio, H. J. Mamin, C. T. Rettner, and D. Rugar, Proceedings of the National Academy of Sciences **106**, 1313 (2009).

[24] Y. Huang and H. J. Maris, Journal of Low Temperature Physics **186**, 208 (2017).

[25] P. McClintock, Physics Letters A **29**, 453 (1969).

[26] A. D. Kashkanova, A. B. Shkarin, C. D. Brown, N. E. Flowers-Jacobs, L. Childress, S. W. Hoch, L. Hohmann, K. Ott, J. Reichel, and J. G. E. Harris, Nature Physics **13**, 74 (2017).

[27] H. J. Mamin, R. Budakian, B. W. Chui, and D. Rugar, Physical Review Letters **91**, 207604 (2003).

[28] E. Leirset, H. E. Engan, and A. Aksnes, Optics Express **21**, 19900 (2013).

[29] A. B. Shkarin, A. D. Kashkanova, C. D. Brown, S. Garcia, K. Ott, J. Reichel, and J. G. E. Harris, Physical Review Letters **122**, 153601 (2019).

[30] D. Hunger, C. Deutsch, R. J. Barbour, R. J. Warburton, and J. Reichel, AIP Advances **2**, 012119 (2012).

[31] See supplemental material.

[32] S. Nimmrichter, K. Hammerer, P. Asenbaum, H. Ritsch, and M. Arndt, New Journal of Physics **12**, 083003 (2010).

[33] N. Kiesel, F. Blaser, U. Delic, D. Grass, R. Kaltenbaek, and M. Aspelmeyer, Proceedings of the National Academy of Sciences **110**, 14180 (2013).

[34] M. Aspelmeyer, T. J. Kippenberg, and F. Marquardt, Reviews of Modern Physics **86**, 1391 (2014).

[35] G. Baym, R. G. Barrera, and C. J. Pethick, Physical Review Letters **22**, 20 (1969).

[36] L. Kramer, Physical Review A **1**, 1517 (1970).

[37] A. F. Borghesani, *Ions and Electrons in Liquid Helium*, International Series of Monographs on Physics No. 137 (Oxford University Press, Oxford ; New York, 2007).

[38] U. Grob, M. D. Krass, M. Héritier, R. Pachlatko, J. Rhensius, J. Košata, B. A. Moores, H. Takahashi, A. Eichler, and C. L. Degen, Nano Letters **19**, 7935 (2019).

A proposal for detecting the spin of a single electron in superfluid helium

Jinyong Ma,[1] Y. S. S. Patil,[1] Jiaxin Yu,[2] Yiqi Wang,[2] and J. G. E. Harris[1, 2, 3, *]

[1]*Department of Physics, Yale University, New Haven, Connecticut 06520, USA*
[2]*Department of Applied Physics, Yale University, New Haven, Connecticut 06520, USA*
[3]*Yale Quantum Institute, Yale University, New Haven, Connecticut 06520, USA*

This supplemental material presents detailed calculations for the analyses in the main paper. Section I provides the theory for acoustic trapping of an electron bubble. Section II discusses the optomechanical interaction between an electron bubble and an optical mode. Section III estimates the mechanical damping of the bubble motion. Section IV gives details of the three protocols for single-spin detection proposed in the main paper. Section V analyzes the noise sources influencing the system performance. Section VI lists the various parameters used in the calculations.

CONTENTS

I. SOUND WAVE TRAPPING

A. Energy and Young's modulus of electron bubbles

We consider the following simple model for describing the total energy of an electron bubble (EB) in liquid helium [1–4]

$$E_{\text{tol}} = \frac{h^2}{8m_e R^2} + 4\pi R^2 \sigma + \frac{4}{3}\pi R^3 P \tag{1}$$

where the first term is the ground state energy of the confined electron, the second term is the surface tension energy of the bubble, and the last term represents the energy stored by the surrounding pressure (a more sophisticated model is described in Ref. [2]). Here the electron mass is m_e, the bubble radius is R, the surface tension of liquid helium is $\sigma = 0.375$ erg/cm^2 [5], and the pressure experienced by the EB is P. When $P = 0$, the EB radius is found by minimizing the total energy with respect to R, giving:

$$R_0 = \left(\frac{h^2}{32\pi m_e \sigma}\right)^{1/4} \approx 1.9 \text{ nm} \tag{2}$$

To find the response of the EB to an acoustic wave in the surrounding liquid, we rewrite Eq. (1) as

$$P = \frac{h^2}{16\pi m_e}\left(\frac{3}{4\pi}V_{\text{EB}}\right)^{-5/3} - 2\sigma\left(\frac{3}{4\pi}V_{\text{EB}}\right)^{-1/3} \tag{3}$$

where $V_{\text{EB}} = 4\pi R^3/3$ is the volume of the EB. It is then straightforward to calculate the Young's modulus (E_{EB}) of the EB:

$$E_{\text{EB}} = -V_{\text{EB}}\frac{\partial P}{\partial V_{\text{EB}}} \approx 530 \text{ kPa} \tag{4}$$

B. Potential of an acoustic trap

An EB in a standing acoustic wave experiences a force exerted by the acoustic field. As described in the main text, our proposal employs this force to trap the EB. The potential energy of an EB in an acoustic wave (with wave vector k) can be written as [6]

$$U_{\text{ac}} = V_{\text{EB}}W_{\text{ac}}\left[f_1 \cos^2(kz) - \frac{3f_2}{2}\sin^2(kz)\right]$$
$$= V_{\text{EB}}W_{\text{ac}}\left[f_1 - \Phi\sin^2(kz)\right] \tag{5}$$

where z is the coordinate of the EB along the cavity axis (see Fig. 1 of the main text), and

$$f_1 = 1 - \frac{E_{\text{He}}}{E_{\text{EB}}} \tag{6}$$

$$f_2 = \frac{2(\rho_{\text{EB}}/\rho_{\text{He}} - 1)}{2\rho_{\text{EB}}/\rho_{\text{He}} + 1} \tag{7}$$

$$\Phi = f_1 + \frac{3}{2}f_2 \tag{8}$$

Here W_{ac} is the acoustic energy density (see below), and the Young's modulus of the liquid He is $E_{\text{He}} = \rho_{\text{He}}c_{\text{He}}^2$ where $c_{\text{He}} = 238$ m/s is the velocity of sound in liquid He and $\rho_{\text{He}} = 145$ kg/m^3 is its mass density. Since the interior of the EB is close to vacuum, we take its mass density $\rho_{\text{EB}} = 0$. This gives $f_1 \approx -14$, $f_2 \approx -2$, and $\Phi \approx -17$. The quantity Φ is known as the acoustophoretic contrast factor, and its sign determines whether the bubble is trapped at the pressure nodes or antinodes of the acoustic wave. Here $\Phi < 0$, so the EB will be trapped at pressure antinodes.

The depth of the trapping potential in Eq. (5) is $U_0 = V_{\text{EB}}\Phi W_{\text{ac}}$. Throughout this paper, we assume $U_0/k_B = 300$ mK (chosen to be 10× greater than the assumed operating temperature $T = 30$ mK). This corresponds to an acoustic energy density of $W_{\text{ac}} = 8.5$ J/m^3. Generating such an acoustic wave is discussed in Section I C.

To find the trap frequency of the EB, we expand U_{ac} to second order in z around its minimum at z_0, i.e.

$$U(z_0 + \delta z) \approx U(z = z_0) + \frac{1}{2}U''(z = z_0)\delta z^2$$
$$= V_{\text{EB}}W_{\text{ac}}f_1 + \frac{1}{2}k_{\text{EB}}\delta z^2 \tag{9}$$

where $k_{\text{EB}} = -2V_{\text{EB}}W_{\text{ac}}k^2\Phi\cos(2kz_0)$ is the spring constant of the trap. This results in a trap frequency $\omega_{\text{EB}} = \sqrt{k_{\text{EB}}/m_{\text{EB}}} \approx 2\pi \times 2.9$ MHz along the z-direction (here $m_{\text{EB}} = 1.6 \times 10^{-24}$ kg is the bubble's effective mass [7]).

C. Generation of the acoustic trap with a piezoelectric actuator

The acoustic wave is generated by vibrating one of the cavity fibers with a piezoelectric actuator at frequency ω_{ac}. If the fiber displacement is $z_f = z_{amp} \sin(\omega_{ac}t)$, the power in the sound wave ($\mathcal{P}_{ac}$) emitted into the liquid helium is [8]

$$
\begin{aligned}
\mathcal{P}_{ac} &= \sigma_{rad}\rho_{He}c_{He}A \left\langle v^2 \right\rangle \\
&= \sigma_{rad}\rho_{He}c_{He}A \left\langle \left(z_{amp}\omega_{ac}\cos(\omega_{ac}t) \right)^2 \right\rangle \\
&= \frac{\sigma_{rad}\rho_{He}c_{He}A\omega_{ac}^2 z_{amp}^2}{2}
\end{aligned}
\tag{10}
$$

where σ_{rad} is the radiation ratio (or efficiency), v is the speed of the fiber tip of area A, and $\langle \cdot \rangle$ denotes the time average. $\mathcal{P}_{ac}$ can also be written in terms of sound pressure or acoustic energy density

$$
\mathcal{P}_{ac} = 2AW_{ac}c_{He}
\tag{11}
$$

We obtain the required vibration amplitude by combining Eqs. (10)-(11).

$$
z_{amp} = \sqrt{\frac{4W_{ac}}{\sigma_{rad}\rho_{He}\omega_{ac}^2}}
\tag{12}
$$

Thus, to produce a sound wave that results in a trap depth corresponding to 300 mK (see Sec 1.2), the amplitude of the fiber motion would need to be $z_{amp} \approx 240$ pm. However if the fiber motion is resonant with an acoustic mode of the cavity, this is reduced by a factor of the acoustic mode's quality factor Q_{ac}. For the devices demonstrated in Ref. [9, 10], $Q_{ac} \approx 10^5$. As a result, the required $z_{amp} \approx 2.4$ fm. This amount of motion at comparable frequency is demonstrated, for example in [11].

D. Detection of the acoustic trap

We first look at the acoustic energy stored in the fiber cavity $\mathcal{E}_{ac}$, which is given by [12]

$$
\mathcal{E}_{ac} = \frac{1}{2}E_{He} \int \left| \frac{\delta\rho_{He}(r)}{\rho_{He}} \right|^2 dV = \frac{1}{2E_{He}} \int |P(r)|^2 \, dV
\tag{13}
$$

where $P(r)$ is the pressure profile of the acoustic mode, and $\delta\rho_{He}(r)$ is the corresponding density variation. Using $W_{ac} = \frac{P_0^2}{4E_{He}}$ [6] (where P_0 is the amplitude of the acoustic mode), and the well-known mode profiles for a Fabry-Perot cavity, we can write the time-averaged acoustic energy as

$$
\langle \mathcal{E}_{ac} \rangle = \frac{1}{2}W_{ac}V_{ac}
\tag{14}
$$

with V_{ac} denoting the mode volume of the acoustic cavity.

The acoustic energy can also be written in terms of the phonon number n_{ac}

$$
\langle \mathcal{E}_{ac} \rangle = \left(n_{ac} + \frac{1}{2} \right)\hbar\omega_{ac}
\tag{15}
$$

Equations (13)-(15) provide the phonon number ($n_{ac} \approx 1.6 \times 10^{11}$) and the corresponding amplitude of the helium density variation ($\frac{\delta\rho_{He}}{\rho_{He}} \approx 2 \times 10^{-3}$) required to achieve the trap depth (300 mK) for the acoustic mode with $\omega_{ac}/2\pi = 320$ MHz, as considered in the main text.

The acoustic trap can be optically detected using the optomechanical interaction between the optical and acoustic modes of the fiber cavity. Under the drive of a monochromatic laser with frequency ω_l and amplitude c_l, the equations of motion for the amplitudes c and d of the optical and acoustic modes (with resonance frequencies ω_c and ω_{ac}, and dampings κ and γ_{ac}) can be written in the rotating frame of ω_l as [12, 13],

$$
\dot{c} = -\left(\frac{\kappa}{2} - i\bar{\Delta} \right)c + \sqrt{\kappa_{ex}}c_l,
\tag{16}
$$

$$
\dot{d} = -\left(\frac{\gamma_{ac}}{2} + i\omega_{ac} \right)d - ig_{0,ac}c^\dagger c + d_{ext}e^{-i\omega_{ac}t}
\tag{17}
$$

where $\Delta_l = \omega_l - \omega_c$. Here we define the effective cavity detuning as $\bar{\Delta} = \Delta_l - ig_{0,\mathrm{ac}}(d + d^\dagger)$ and denote d_{ext} as the external acoustic drive applied by the fiber vibration. The laser is injected into the cavity with input coupling rate κ_{ex}, and the single-photon optomechanical coupling rate is $g_{0,\mathrm{ac}}$. We consider a weak probe beam such that the radiation pressure on the acoustic wave is ignored. Eq.17 is then

$$\dot{d} = -\left(\frac{\gamma_{\mathrm{ac}}}{2} + i\omega_{\mathrm{ac}}\right)d + d_{\mathrm{ext}}e^{-i\omega_{\mathrm{ac}}t} \tag{18}$$

The solution to this equation is simply $d = d_1 e^{-i\omega_{ac}t}$, where $d_1 = 2d_{\mathrm{ext}}/\gamma_{\mathrm{ac}}$.

In this analysis, the optical resonance frequency is modulated with a depth $g_{0,\mathrm{ac}}(d_1 + d_1^\dagger)$. With $d_1 = \sqrt{n_{\mathrm{ac}}} \approx 4 \times 10^5$ and the device parameters considered here ($\kappa/2\pi = 15$ MHz, $L_{\mathrm{cav}} = 100\,\mu$m, $\mathcal{F}_{\mathrm{opt}} = 10^5$, $g_{0,\mathrm{ac}}/2\pi = 3.6$ kHz), the cavity modulation depth $\approx 190\kappa$.

II. INTERACTION BETWEEN ELECTRON BUBBLE AND CAVITY OPTICAL FIELD

Since the electron bubble radius ($R_0 \approx 1.9$ nm) is much smaller than the optical wavelength ($\lambda_{\mathrm{opt}} = 1550$ nm), the Hamiltonian for a bubble coupling to the optical field (with frequency ω_c) can be written as [14, 15]

$$H = -\frac{1}{2}\alpha\,|E|^2 = -\frac{\hbar\omega_c\alpha}{2\varepsilon_{\mathrm{He}}V_{\mathrm{opt}}}f(z)a^\dagger a \tag{19}$$

$$\tag{20}$$

where the EB polarizability is

$$\alpha = 3\varepsilon_{\mathrm{He}}V_{\mathrm{EB}}\mathrm{Re}\left\{\frac{n_{\mathrm{EB}}^2/n_{\mathrm{He}}^2 - 1}{n_{\mathrm{EB}}^2/n_{\mathrm{He}}^2 + 2}\right\} \tag{21}$$

and $n_{\mathrm{EB}} = 1$ and $n_{\mathrm{He}} = 1.028$ are the refractive indices of the EB and the liquid He, $\epsilon_{\mathrm{He}} \approx n_{\mathrm{He}}^2$ is the permittivity of liquid He, and V_{opt} is the mode volume of the optical cavity. Here $f(z)$ is the profile of the optical cavity mode along the z direction, given by

$$f(z) = \frac{1}{1 + (z_0 + z)^2/z_{\mathrm{R}}^2}\cos^2\left(k_{\mathrm{opt}}(z_0 + z)\right)$$
$$\approx \cos^2\left(k_{\mathrm{opt}}z_0\right) - k_{\mathrm{opt}}\sin(2k_{\mathrm{opt}}z_0)z - k_{\mathrm{opt}}^2\cos(2k_{\mathrm{opt}}z_0)z^2 + O(z^3) \tag{22}$$

with $k_{\mathrm{opt}} = 2\pi/\lambda_{\mathrm{opt}}$. The pre-factor $\frac{1}{1+(z/z_R)^2} \approx 1$ for the cavities considered in Ref. [13]. The term proportional to z leads to the usual linear optomechanical interaction

$$H = \hbar g_0 a^\dagger a(b^\dagger + b) \tag{23}$$

with

$$g_0 = \frac{\omega_c\alpha k_{\mathrm{opt}}}{2\varepsilon_{\mathrm{He}}V_{\mathrm{opt}}}\sin(2k_{\mathrm{opt}}z_0)z_{\mathrm{zpf}} \tag{24}$$

where $z_{\mathrm{zpf}} = \sqrt{\frac{\hbar}{2m_{\mathrm{EB}}\omega_{\mathrm{EB}}}}$ is the zero point motion of the EB, $z = z_{\mathrm{zpf}}(b + b^\dagger)$, and b denotes the annihilation operator of the EB motion. As discussed in the main paper, the equilibrium position of the trapped bubble corresponds to zero optomechanical coupling of the optical mode used to detect the acoustic trap. To maximize the coupling rate to the EB motion, one can use a different optical mode. The phase difference in the expression for g_0 (see Eq. 24) for two optical modes of wavenumbers k_{q+n} and k_q (i.e. of longitudinal indices $q + n$ and q) at the same location z_0 is

$$2(k_{q+n} - k_q)z_0 = \frac{2\pi n}{L_{\mathrm{cav}}}z_0 \tag{25}$$

Considering an adjacent optical mode, i.e., $n = 1$, the phase difference is $\pi/2$ at $z_0 = L_{\mathrm{cav}}/4$, which maximizes the coupling rate.

III. DAMPING MECHANISM

For the temperature range considered in this paper, the damping of the EB motion is expected to be dominated by two sources: collisions with thermal phonons, and collisions with ^{3}He impurities. We estimate the damping rates arising from each of these sources by using the results of Ref. [16] (for the phonons) and Ref. [17] (for the ^{3}He).

In particular, the EB's phonon-limited mobility μ_p is given by Eq. (8) and Eq. (9) of Ref. [16], and the ^{3}He-limited mobility μ_h is given by the expressions in the first portion of Section III of Ref. [17]. These mobilities are then converted to damping rates via $\gamma_{p,h} = e/m\mu_{p,h}$.

In Fig. (1S), the blue curve shows the phonon contribution to the damping (calculated with $R_0 = 1.9$ nm, rather than the slightly smaller value assumed in Ref. [16]), and the red curves show the ^{3}He contribution for a range of x_3 (the concentration of ^{3}He). The total EB damping $\gamma_{EB} = \gamma_h + \gamma_p$ is converted to $Q_{EB} = \omega_{EB}/\gamma_{EB}$ and is shown in Fig. 3 of the main paper (as red curves) for the same values of x_3.
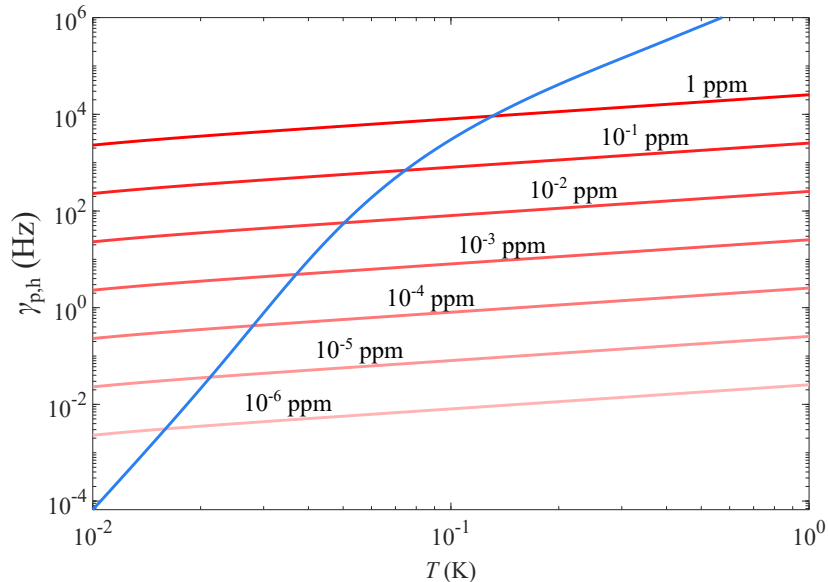
FIG. 1S. Damping rate of the electron bubble's motion. The contribution from thermal phonons (blue) and various concentrations of ^{3}He impurities (red) are shown, both as a function of temperature.

IV. SINGLE SPIN DETECTION

As discussed in the main text, the EB experiences a force along the z direction given by:

$$F_{mag} = \mu_S G \tag{26}$$

where $\mu_S = -g\mu_B/2$ is the z-component of the electron's spin magnetic moment, μ_B and g denote the Bohr magneton and gyromagnetic ratio of the electron, and G is the gradient (with respect to z) of the z component of the magnetic field.

In the following subsections, we will consider three approaches to obtain an alternating magnetic force that drives the bubble motion on resonance.

A. Modulation of magnetic gradient

Modulating the magnetic gradient at the trap frequency is the most straightforward approach to drive the EB's motion resonantly. In this case, the magnetic force is simply

$$F_{mag} = \mu_S G \cos(\omega_{EB} t + \phi) \tag{27}$$

as described in the main text.

B. Rabi oscillation

In this subsection, we consider using Rabi oscillations to produce the oscillating force. We consider the following magnetic field:

$$\vec{B} = \bar{B}_0 \hat{z} + B_1 \left(\cos(\omega t)\hat{x} - \sin(\omega t)\hat{y} \right) \tag{28}$$

where $\bar{B}_0$ is used to induce the Zeeman splitting and B_1 is the amplitude of the microwaves that drive the spin resonance. The Hamiltonian of the system can be expressed as

$$H = -\vec{\mu} \cdot \vec{B} = -\frac{\hbar}{2}\omega_0 \sigma_z - \frac{\hbar}{2}\omega_1 \left(\sigma_x \cos(\omega t) - \sigma_y \sin(\omega t) \right) \tag{29}$$

with $\omega_0 = \frac{\mu_{\mathrm{B}} g}{\hbar}\bar{B}_0$ and $\omega_1 = \frac{\mu_{\mathrm{B}} g}{\hbar}B_1$. Here $\vec{\mu} = -\frac{1}{2}g\mu_{\mathrm{B}}(\sigma_x \hat{x} + \sigma_y \hat{y} + \sigma_z \hat{z})$ where $\sigma_{x,y,z}$ are the Pauli matrices.

If the electron is initially in state $|\downarrow\rangle$, then the probability of the electron being found in spin $|\uparrow\rangle$ is given by

$$P(t) = \left(\frac{\omega_1}{\Omega}\right)^2 \sin^2\left(\frac{\Omega t}{2}\right) \tag{30}$$

Here $\Omega = \sqrt{\Delta^2 + \omega_1^2}$ is the Rabi frequency where $\Delta = \omega - \omega_0$ is the detuning of the microwaves from the spin resonance. Assuming the initial magnetic moment is $\mu_{\mathrm{S},0}$, we have the equation for magnetic force as follows

$$F_{\mathrm{mag}} = \mu_{\mathrm{S},0}P(t)G \tag{31}$$

It is straightforward to tune B_1 and Δ so that $\Omega = \omega_{\mathrm{EB}}$, producing an alternating force whose frequency is ω_{EB}.

C. Adiabatic spin flip

The last approach follows the protocol of Ref. [18, 19], and involves the modulation of $\bar{B}_0$ at frequency ω_{EB} and amplitude B_{mod}. The microwave field for this protocol is resonant for $\bar{B}_0$, i.e. $\omega = \omega_0 = \frac{\mu_{\mathrm{B}} g}{\hbar}\bar{B}_0$. The overall magnetic field is

$$\vec{B} = \left(\bar{B}_0 + B_{\mathrm{mod}} \sin(\omega_{\mathrm{EB}}t) \right)\hat{z} + B_1 \left(\cos(\omega_0 t)\hat{x} - \sin(\omega_0 t)\hat{y} \right) \tag{32}$$

Resulting in the following Hamiltonian:

$$H = -\vec{\mu} \cdot \vec{B} = -\frac{\hbar}{2}\left(\omega_0 + \omega_{\mathrm{mod}} \sin(\omega_{\mathrm{EB}}t) \right)\sigma_z - \frac{\hbar}{2}\omega_1 \left(\sigma_x \cos(\omega_0 t) - \sigma_y \sin(\omega_0 t) \right)$$

with $\omega_{\mathrm{mod}} = \frac{\mu_{\mathrm{B}} g}{\hbar}B_{\mathrm{mod}}$. For convenience, we rewrite this equation in the frame rotating at ω_0:

$$H' = -\frac{\hbar}{2}\omega_{\mathrm{mod}} \sin(\omega_{\mathrm{EB}}t)\sigma_z - \frac{\hbar}{2}\omega_1 \sigma_x \tag{33}$$

If the time-dependence of the Hamiltonian in Eq. (33) is slow enough that the spin state evolves adiabatically, then the z component of the magnetization is [18]

$$\mu_{\mathrm{s}}(t) = \pm \frac{B_{\mathrm{mod}} \sin(\omega_{\mathrm{EB}}t)}{\sqrt{B_1^2 + B_{\mathrm{mod}}^2 \sin(\omega_{\mathrm{EB}}t)^2}}\mu_{\mathrm{eff}} \tag{34}$$

where $\mu_{\mathrm{eff}} = \frac{1}{2}g\mu_{\mathrm{B}}$, and the magnetic force along the z direction is simply

$$F_{\mathrm{mag}} = \mu_{\mathrm{s}}(t)G \tag{35}$$

To estimate the probability that the spin evolves adiabatically under the in Eq. (33), we model each passage through the avoided crossing (which occurs when $t = n\pi/\omega_{\mathrm{EB}}$, with n an integer) using the Landau-Zener formula. Specifically, we replace $\sin(\omega_{\mathrm{EB}}t)$ in Eq. (33) with $\omega_{\mathrm{EB}}t$, so that the resulting Hamiltonian is equivalent to

$$H' = \frac{1}{2}\alpha t \sigma_z + \mathrm{Re}(H_{12})\sigma_x - \mathrm{Im}(H_{12})\sigma_y \tag{36}$$

where $H_{12} = -\frac{\hbar}{2}\omega_1$ and $\alpha = -\hbar\omega'\omega_{\mathrm{mod}}$. In this case, the probability to find the system in the state $|\uparrow\rangle$ at $t = \infty$ given that the system is in the state $|\uparrow\rangle$ at $t = -\infty$ is the well-known expression

$$P_{\mathrm{LZ}}(\uparrow|\uparrow) = \exp\left(-2\pi\frac{|H_{12}|^2}{\hbar|\alpha|}\right) = \exp\left(-\frac{\pi}{2}\frac{\omega_1^2}{\omega_{\mathrm{EB}}\omega_{\mathrm{mod}}}\right) \tag{37}$$

As a result, the probability that the spin state evolves adiabatically (and hence the Eq. (34) holds) is $1 - P_{\mathrm{LZ}}(\uparrow|\uparrow)$. This probability approaches unity when $\omega_{\mathrm{EB}}\omega_{\mathrm{mod}} \ll \omega_1^2$.

Equation (37) is used to calculate the probability of adiabatic evolution given in Fig. 4(c,d) of the main text.

V. NOISE ANALYSIS

In this section, we start with the equations of motion for the EB and the optical mode and analyse the noise sources associated with measuring the EB displacement.

A. Optomechanical interaction

The Hamiltonian describing the system can be written as

$$H = \hbar\omega_c a^\dagger a + \hbar\omega_{\mathrm{EB}}b^\dagger b + \hbar g_0 a^\dagger a(b^\dagger + b) + F_{\mathrm{mag}}x_{\mathrm{zpf}}(b^\dagger + b) \tag{38}$$

The first three terms characterize the optical mode of the fiber cavity, the EB motion, and their interaction, respectively. The last term describes the magnetic force imprinted from the electron spin [20]. Adding the optical (κ) and mechanical (γ_{EB}) damping terms and environmental fluctuations, the Heisenberg equations of motion are

$$\dot{a} = -\left(\frac{\kappa}{2} + i\omega_c\right)a - ig_0(b^\dagger + b)a + \sqrt{\kappa_{\mathrm{in}}}\xi_{\mathrm{in}} + \sqrt{\kappa_{\mathrm{ex}}}(a_{\mathrm{ex}} + \xi_{\mathrm{ex}}) \tag{39}$$

$$\dot{b} = -\left(\frac{\gamma_{\mathrm{EB}}}{2} + i\omega_{\mathrm{EB}}\right)b - ig_0 a^\dagger a - \frac{i}{\hbar}F_{\mathrm{mag}}x_{\mathrm{zpf}} + \sqrt{\gamma_{\mathrm{EB}}}\eta \tag{40}$$

where ξ_{in} and ξ_{ex} denote the optical noises coupled to the system via internal and external channels with the corresponding coupling rates κ_{in} and κ_{ex}. We have also included the mechanical noise η that comes from the thermal bath. The noise operators' correlations are

$$\left\langle \xi_i(t)\xi_j(t')\right\rangle = 0 \tag{41}$$

$$\left\langle \xi_i^\dagger(t)\xi_j(t')\right\rangle = 0 \tag{42}$$

$$\left\langle \xi_i(t)\xi_j^\dagger(t')\right\rangle = \delta_{ij}\delta(t - t') \tag{43}$$

$$\left\langle \eta(t)\eta(t')\right\rangle = 0 \tag{44}$$

$$\left\langle \eta^\dagger(t)\eta(t')\right\rangle = n_{\mathrm{th}}\delta(t - t') \tag{45}$$

$$\left\langle \eta(t)\eta^\dagger(t')\right\rangle = (n_{\mathrm{th}} + 1)\delta(t - t') \tag{46}$$

where n_{th} is the thermal phonon occupancy of the EB's motion.

We consider a monochromatic optical drive, i.e., $a_{\mathrm{ex}} = a_l e^{-i\omega_l t}$. In the frame rotating at ω_c, we rewrite Eqs. (39) and (40) as

$$\dot{a} = -\frac{\kappa}{2}a - ig_0(b^\dagger + b)a + \sqrt{\kappa_{\mathrm{in}}}\xi_{\mathrm{in}} + \sqrt{\kappa_{\mathrm{ex}}}\xi_{\mathrm{ex}} + \sqrt{\kappa_{\mathrm{ex}}}a_l e^{-i\Delta_l t} \tag{47}$$

$$\dot{b} = -\left(\frac{\gamma_{\mathrm{EB}}}{2} + i\omega_{\mathrm{EB}}\right)b - ig_0 a^\dagger a - \frac{i}{\hbar}F_{\mathrm{mag}}x_{\mathrm{zpf}} + \sqrt{\gamma_{\mathrm{EB}}}\eta \tag{48}$$

where $\Delta_l = \omega_l - \omega_c$. Applying the linearization: $a \to a_0 + a$ and $b \to b_0 + b$, we get the zeroth-order equations

$$\dot{a_0} = -\frac{\kappa}{2}a_0 - ig_0(b_0^* + b_0)a_0 + \sqrt{\kappa_{\mathrm{ex}}}a_l e^{-i\Delta_l t} \tag{49}$$

$$\dot{b_0} = -\left(\frac{\gamma_{\mathrm{EB}}}{2} + i\omega_{\mathrm{EB}}\right)b_0 - iga_0^* a_0 \tag{50}$$

and the first-order equations

$$\dot{a} = -\frac{\kappa}{2}a - ig_0(a_0b^\dagger + a_0b + b_0^*a + b_0a) + \sqrt{\kappa_{\text{in}}}\xi_{\text{in}} + \sqrt{\kappa_{\text{ex}}}\xi_{\text{ex}} \tag{51}$$

$$\dot{b} = -\left(\frac{\gamma_{\text{EB}}}{2} + i\omega_{\text{EB}}\right)b - ig_0(a_0^*a + a^\dagger a_0) - \frac{i}{\hbar}F_{\text{mag}}x_{\text{zpf}} + \sqrt{\gamma_{\text{EB}}}\eta \tag{52}$$

The zero-order solutions for the optical and mechanical modes are:

$$a_0 = \frac{\sqrt{\kappa_{\text{ex}}}a_l}{\kappa/2 - i\bar{\Delta}}e^{-i\Delta_l t} \tag{53}$$

$$b_0 = \frac{-iga_0^*a_0}{\frac{\gamma_{\text{EB}}}{2} + i\omega_{\text{EB}}} \tag{54}$$

where $\bar{\Delta} = \Delta_l - g_0(b_0^* + b_0)$. The reduced first-order equations are

$$\dot{a} = -\frac{\kappa}{2}a - ig_0a_0(b^\dagger + b) + \sqrt{\kappa}\xi \tag{55}$$

$$\dot{b} = -\left(\frac{\gamma_{\text{EB}}}{2} + i\omega_{\text{EB}}\right)b - ig_0(a_0^*a + a^\dagger a_0) - \frac{i}{\hbar}F_{\text{mag}}x_{\text{zpf}} + \sqrt{\gamma_{\text{EB}}}\eta \tag{56}$$

where we have introduced a combined vacuum noise operator,

$$\xi = (\sqrt{\kappa_{\text{in}}}\xi_{\text{in}} + \sqrt{\kappa_{\text{ex}}}\xi_{\text{ex}})/\sqrt{\kappa} \tag{57}$$

Equations (55) and (56) can be written in the frequency domain as follows

$$a[\omega] = \chi_c[\omega]\left(-ig_0a_0(b^\dagger[\omega - \Delta_l] + b[\omega - \Delta_l]) + \sqrt{\kappa}\xi[\omega]\right) \tag{58}$$

$$b[\omega] = \chi_{\text{m}}[\omega]\left(-ig_0(a_0^*a[\omega + \Delta_l] + a_0a^\dagger[\omega - \Delta_l]) - \frac{i}{\hbar}x_{\text{zpf}}F_{\text{mag}}[\omega] + \sqrt{\gamma_{\text{EB}}}\eta[\omega]\right) \tag{59}$$

Here we use the noise operators' correlations in the frequency domain:

$$\langle\xi(\omega)\xi(-\omega)\rangle = 0 \tag{60}$$

$$\left\langle\xi^\dagger(\omega)\xi(-\omega)\right\rangle = 0 \tag{61}$$

$$\left\langle\xi(\omega)\xi^\dagger(-\omega)\right\rangle = 1 \tag{62}$$

$$\langle\eta(\omega)\eta(-\omega)\rangle = 0 \tag{63}$$

$$\left\langle\eta^\dagger(\omega)\eta(-\omega)\right\rangle = n_{th} \tag{64}$$

$$\left\langle\eta(\omega)\eta^\dagger(-\omega)\right\rangle = n_{th} + 1 \tag{65}$$

Note that $x^\dagger[\omega] = (x[-\omega])^\dagger$. We also define optical and mechanical susceptibility as

$$\chi_c[\omega] = \left(\frac{\kappa}{2} - i\omega\right)^{-1} \tag{66}$$

$$\chi_{\text{m}}[\omega] = \left(\frac{\gamma_{\text{EB}}}{2} - i(\omega - \omega_{\text{EB}})\right)^{-1} \tag{67}$$

The solution to (56) is easily obtained as

$$b[\omega] = \chi_{\text{eff}}[\omega]\left(-i\frac{x_{\text{zpf}}}{\hbar}F_{\text{RPSN}}[\omega] - i\frac{x_{\text{zpf}}}{\hbar}F_{\text{mag}}[\omega] + \sqrt{\gamma_{\text{EB}}}\eta[\omega]\right) \tag{68}$$

$$b^\dagger[\omega] = (\chi_{\text{eff}}[-\omega])^*\left(i\frac{x_{\text{zpf}}}{\hbar}F_{\text{RPSN}}[\omega] + i\frac{x_{\text{zpf}}}{\hbar}F_{\text{mag}}^\dagger[\omega] + \sqrt{\gamma_{\text{EB}}}\eta^\dagger[\omega]\right) \tag{69}$$

with

$$\chi_{\text{eff}}^{-1}[\omega] = \chi_{\text{m}}^{-1}[\omega] + i\Sigma_{\text{opt}}[\omega] \tag{70}$$

$$\Sigma_{\text{opt}}[\omega] = ig_0^2\left(|a_0|^2\chi_c[\omega - \Delta_l] - |a_0|^2\chi_c[\omega + \Delta_l]\right) \tag{71}$$

$$F_{\text{RPSN}}[\omega] = \frac{\hbar}{x_{\text{zpf}}}g_0\sqrt{\kappa}\left(a_0^*\chi_c[\omega + \Delta_l]\xi[\omega + \Delta_l] + a_0\chi_c[\omega - \Delta_l]\xi^\dagger[\omega - \Delta_l]\right) \tag{72}$$

where χ_{eff} is the effective mechanical susceptibility modified by the optical backaction. The optical spring Ω_{opt} and optical damping Γ_{opt} can be extracted from $\Sigma_{\text{opt}}[\omega]$

$$\Omega_{\text{opt}} = \text{Re}\left[\Sigma_{\text{opt}}[\omega]\right] \tag{73}$$

$$\Gamma_{\text{opt}} = -2\text{Im}\left[\Sigma_{\text{opt}}[\omega]\right] \tag{74}$$

The radiation pressure shot noise F_{RPSN} (see Eq. (72)) originates from the backaction of the optical fluctuations. Its power spectral density (PSD) is found using the Wiener-Khinchin theorem

$$
\begin{aligned}
S_{FF}^{\text{RPSN}}[\omega] &= \langle F_{\text{RPSN}}[\omega]F_{\text{RPSN}}[-\omega]\rangle \\
&= \frac{\hbar^2 g_0^2 |a_0|^2}{x_{\text{zpf}}^2} \frac{\kappa}{\kappa^2/4 + (\omega + \Delta_l)^2}
\end{aligned}
\tag{75}
$$

With the correlations of thermal noise operators given in Eqs. (64)-(65), we can easily get the PSD of thermal fluctuation

$$S_{F^\dagger F}^{\text{th}}[\omega] = \frac{\hbar^2}{x_{\text{zpf}}^2}\left\langle \sqrt{\gamma_{\text{EB}}}\eta^\dagger[\omega]\sqrt{\gamma_{\text{EB}}}\eta[-\omega]\right\rangle = \frac{\hbar^2}{x_{\text{zpf}}^2}\gamma_{\text{EB}}n_{\text{th}} \tag{76}$$

$$S_{FF^\dagger}^{\text{th}}[\omega] = \frac{\hbar}{x_{\text{zpf}}}\left\langle \sqrt{\gamma_{\text{EB}}}\eta[\omega]\sqrt{\gamma_{\text{EB}}}\eta^\dagger[-\omega]\right\rangle = \frac{\hbar^2}{x_{\text{zpf}}^2}\gamma_{\text{EB}}(n_{\text{th}} + 1) \tag{77}$$

The difference in $S_{F^\dagger F}^{\text{th}}[\omega]$ and $S_{FF^\dagger}^{\text{th}}[\omega]$ will lead to the well-known quantum phenomenon called sideband asymmetry [21]. These two equations can be rewritten as follows for large thermal occupations

$$S_{F^\dagger F}^{\text{th}}[\omega] \approx S_{FF^\dagger}^{\text{th}}[\omega] \approx 2k_B T m_{\text{EB}}\gamma_{\text{EB}} \tag{78}$$

Here we have used $n_{\text{th}} \approx k_B T/\hbar\omega_{\text{EB}}$. Equations (68) and (69) suggest the following PSD for the mechanical mode

$$S_{b^\dagger b}[\omega] = |\chi_{\text{eff}}[-\omega]|^2 \frac{x_{\text{zpf}}^2}{\hbar^2}\left(S_{FF}^{\text{RPSN}}[\omega] + S_{FF}^{\text{mag}}[\omega] + S_{F^\dagger F}^{\text{th}}[\omega]\right) \tag{79}$$

$$S_{bb^\dagger}[\omega] = |\chi_{\text{eff}}[\omega]|^2 \frac{x_{\text{zpf}}^2}{\hbar^2}\left(S_{FF}^{\text{RPSN}}[\omega] + S_{FF}^{\text{mag}}[\omega] + S_{FF^\dagger}^{\text{th}}[\omega]\right) \tag{80}$$

Because $x[\omega] = x_{\text{zpf}}(b[\omega] + b^\dagger[\omega])$, we obtain the PSD of the mechanical displacement

$$
\begin{aligned}
S_{xx}[\omega] &= x_{\text{zpf}}^2\left(S_{bb^\dagger}[\omega] + S_{b^\dagger b}[\omega]\right) \\
&= |\chi_{\text{eff}}[-\omega]|^2 \frac{1}{4m^2\omega_{\text{EB}}^2}\left(S_{FF}^{\text{RPSN}}[\omega] + S_{FF}^{\text{mag}}[\omega] + S_{F^\dagger F}^{\text{th}}[\omega]\right) \\
&\quad + |\chi_{\text{eff}}[\omega]|^2 \frac{1}{4m^2\omega_{\text{EB}}^2}\left(S_{FF}^{\text{RPSN}}[\omega] + S_{FF}^{\text{mag}}[\omega] + S_{FF^\dagger}^{\text{th}}[\omega]\right)
\end{aligned}
\tag{81}
$$

Having found the solution for $b[\omega]$, the solution of the intracavity field in Eq. (55) is obtained. With the input-output relation $a_{\text{out}}[\omega] = \sqrt{\kappa_{\text{ex}}}a[\omega]$, we find the PSD for the cavity output as

$$S_{a^\dagger a}^{\text{out}}[\omega] = \kappa_{\text{ex}}\left\langle a^\dagger[\omega]a[-\omega]\right\rangle \tag{82}$$

$$= \kappa_{\text{ex}}|\chi_c[-\omega]|^2 g_0^2 |a_0|^2 \left(S_{b^\dagger b}[\omega + \Delta_l] + S_{bb^\dagger}[\Delta_l + \omega]\right) \tag{83}$$

B. Heterodyne detection

Here we consider optical heterodyne detection. The optical field a_{det} incident on a photodiode includes the cavity output and local oscillator, which is given by

$$a_{\text{det}} = a_{\text{lo}}e^{i\omega_{\text{lo}}t} + a \tag{84}$$

where a_{lo} and ω_{lo} denote the amplitude and frequency of the local oscillator. The autocorrelation of the photocurrent is

$$G_{ii}(t,\tau) = \langle i(t+\tau/2)i(t-\tau/2)\rangle$$

$$= G^2 \left\langle : a_{\det}^\dagger(t+\tau/2)a_{\det}(t+\tau/2)a_{\det}^\dagger(t-\tau/2)a_{\det}(t-\tau/2) : \right\rangle + G^2 \left\langle a_{\det}^\dagger(t)a_{\det}(t)\right\rangle \delta(\tau)$$

$$\approx G^2 |a_{\rm lo}|^4 + G^2 |a_{\rm lo}|^2 \left\langle a^\dagger(t+\tau/2)a(t+\tau/2)\right\rangle + G^2 |a_{\rm lo}|^2 \left\langle a^\dagger(t-\tau/2)a(t-\tau/2)\right\rangle$$

$$+ G^2 |a_{\rm lo}|^2 \, e^{i\omega_{\rm lo}\tau} \left\langle a^\dagger(t+\tau/2)a(t-\tau/2)\right\rangle + G^2 |a_{\rm lo}|^2 \, e^{-i\omega_{\rm lo}\tau} \left\langle a^\dagger(t-\tau/2)a(t+\tau/2)\right\rangle$$

$$+ G^2 a_{\rm lo}^2 e^{2i\omega_{\rm lo}t} \left\langle a^\dagger(t+\tau/2)a^\dagger(t-\tau/2)\right\rangle + G^2 \left(a_{\rm lo}^*\right)^2 e^{-2i\omega_{\rm lo}t} \langle a(t+\tau/2)a(t-\tau/2)\rangle$$

$$+ G^2 |a_{\rm lo}|^2 \, \delta(\tau) \tag{85}$$

where G is the gain of the detector and the last term represents the detector shot noise. The PSD of the photocurrent is the Fourier transform of the correlation

$$S_{ii}[\omega] = G^2 |a_{\rm lo}|^2 \left(S_{a^\dagger a}[\omega_{\rm lo}+\omega] + S_{a^\dagger a}[\omega_{\rm lo}-\omega] + 1\right)$$

$$= G^2 |a_{\rm lo}|^2 \left(g^2 |a_0|^2 |\chi_c[-(\omega_{\rm lo}+\omega)]|^2 \left(S_{b^\dagger b}[\omega_{\rm lo}+\omega+\Delta_l] + S_{bb^\dagger}[\Delta_l+\omega_{\rm lo}+\omega]\right)\right.$$

$$\left. + g^2 |a_0|^2 |\chi_c[-(\omega_{\rm lo}-\omega)]|^2 \left(S_{b^\dagger b}[\omega_{\rm lo}-\omega+\Delta_l] + S_{bb^\dagger}[\Delta_l+\omega_{\rm lo}-\omega]\right) + 1\right) \tag{86}$$
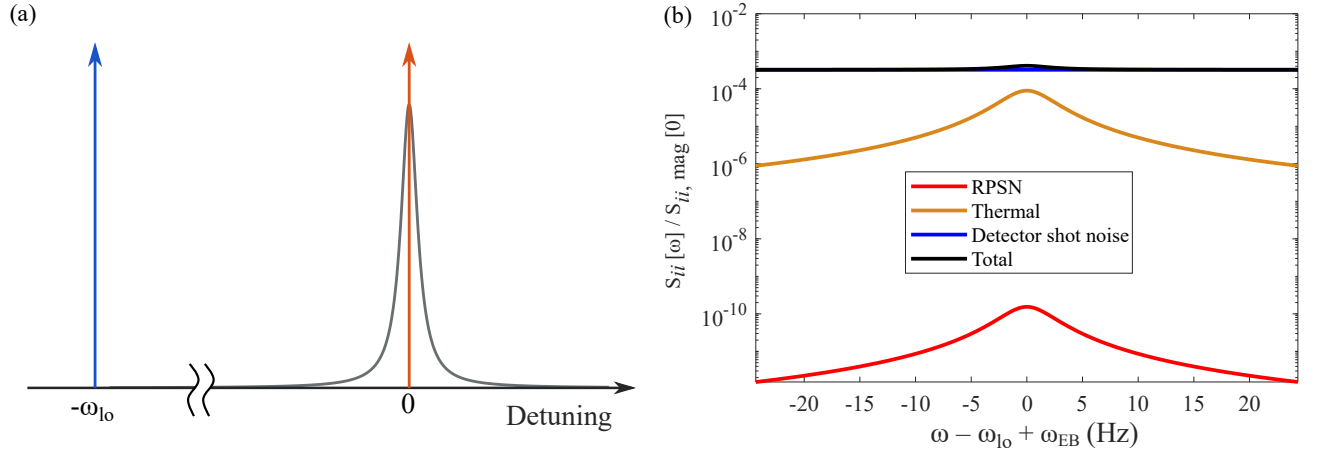

FIG. 2S. (a) Scheme of laser frequencies. The grey curve shows the optical cavity response, while the red arrow represents the probe laser that drives the cavity resonantly. The blue arrow indicates the local oscillator used for the heterodyne readout. (b) The power spectral density $S_{ii}[\omega]$ of the signal recorded by the photo-diode detector, normalized to the magnetic force signal $S_{ii,\rm mag}[0]$ for a measurement bandwidth $b = 1$ Hz. The contributions to S_{ii} from RPSN, the EB's thermal motion, and the measurement noise of the detector are each shown. The parameters used here are: $Q = 6 \times 10^5$, $T = 30$ mK, $P = 1\,\mu$W, $\mathcal{F} = 10^5$.

Figure. 2S(b) shows the contribution to S_{ii} from each noise source, as well as their total.

VI.   TABLE OF PARAMETERS

Optical cavity	
Optical resonant wavelength (λ_{opt})	1550 nm
Optical cavity linewidth ($\kappa/2\pi$)	15 MHz
Optical cavity input coupling rate (κ_{ex})	0.44κ
Cavity Finesse ($\mathcal{F}$)	10^5
Cavity length (L_{cav})	$100\,\mu$m
Cavity waist (w_{cav})	$5\,\mu$m
Operating temperature (T)	30 mK
Acoustic trap	
Acoustic wavelength (λ_{ac})	775 nm
Acoustic resonant frequency ($\omega_{\mathrm{ac}}/2\pi$)	320 MHz
Acoustic optomechanical coupling ($g_{0,\mathrm{ac}}/2\pi$)	3.6 kHz
Quality factor of acoustic mode (Q_{ac})	10^5
Acoustic trap depth (U_0/k_{B})	300 mK
Fiber vibration amplitude (z_{amp})	2.4 fm
Acoustic energy density (W_{ac})	8.5 J/m^3
Phonon number (n_{ac})	1.6×10^{11}
Helium density variation ($\delta\rho_{\mathrm{He}}/\rho_{\mathrm{He}}$)	2×10^{-3}
Optical mode for acoustic wave detection (n_{opt})	129
Acoustic mode number (n_{ac})	258
Electron bubble	
Electron bubble mass (m_{EB})	1.6×10^{-24} kg
Electron bubble radius (R_0)	1.9 nm
Trap frequency ($\omega_{\mathrm{EB}}/2\pi$)	2.9 MHz
Young's modulus of the EB (E_{EB})	530 kPa
Optomechanical coupling rate ($g_0/2\pi$)	0.1 Hz
Cavity mode for EB detection (n_{opt})	130

[1] C. C. Grimes and G. Adams, Physical Review B **41**, 6366 (1990).

[2] J. Classen, C.-K. Su, M. Mohazzab, and H. J. Maris, Physical Review B **57**, 3000 (1998).

[3] D. Konstantinov and H. J. Maris, Physical Review Letters **90**, 025302 (2003).

[4] Y. Xing and H. J. Maris, Journal of Low Temperature Physics **201**, 634 (2020).

[5] P. Roche, G. Deville, N. J. Appleyard, and F. I. B. Williams, Journal of Low Temperature Physics **106**, 565 (1997).

[6] H. Bruus, Lab on a Chip **12**, 1014 (2012).

[7] Y. Huang and H. J. Maris, Journal of Low Temperature Physics **186**, 208 (2017).

[8] H.-S. Han and K.-H. Lee, Journal of Mechanical Science and Technology **28**, 3425 (2014).

[9] A. B. Shkarin, A. D. Kashkanova, C. D. Brown, S. Garcia, K. Ott, J. Reichel, and J. G. E. Harris, Physical Review Letters **122**, 10.1103/PhysRevLett.122.153601 (2019).

[10] A. D. Kashkanova, A. B. Shkarin, C. D. Brown, N. E. Flowers-Jacobs, L. Childress, S. W. Hoch, L. Hohmann, K. Ott, J. Reichel, and J. G. E. Harris, Nature Physics **13**, 74 (2017).

[11] E. Leirset, H. E. Engan, and A. Aksnes, Optics Express **21**, 19900 (2013).

[12] A. Shkarin, *Quantum Optomechanics with Superfluid Helium*, Ph.D. thesis, Yale University (2018).

[13] A. D. Kashkanova, *Optomechanics with Superfluid Helium*, Ph.D. thesis, Yale University (2017).

[14] N. Kiesel, F. Blaser, U. Delic, D. Grass, R. Kaltenbaek, and M. Aspelmeyer, Proceedings of the National Academy of Sciences **110**, 14180 (2013).

[15] S. Nimmrichter, K. Hammerer, P. Asenbaum, H. Ritsch, and M. Arndt, New Journal of Physics **12**, 083003 (2010).

[16] G. Baym, R. G. Barrera, and C. J. Pethick, Physical Review Letters **22**, 20 (1969).

[17] K. W. Schwarz, Physical Review A **6**, 1947 (1972).

[18] H. J. Mamin, R. Budakian, B. W. Chui, and D. Rugar, Physical Review Letters **91**, 207604 (2003).

[19] D. Rugar, R. Budakian, H. J. Mamin, and B. W. Chui, Nature **430**, 329 (2004).

[20] J. Ma, C. You, L.-G. Si, H. Xiong, J. Li, X. Yang, and Y. Wu, Scientific Reports **5**, 11278 (2015).

[21] M. Aspelmeyer, T. J. Kippenberg, and F. Marquardt, Reviews of Modern Physics **86**, 1391 (2014).